

# Characterization of Charge-Carrier Transport in Semicrystalline Polymers: Electronic Couplings, Site Energies, and Charge-Carrier Dynamics in Poly(bithiophene-*alt*-thienothiophene) [PBTTT]

Carl Poelking,<sup>†</sup> Eunkyung Cho,<sup>‡,§</sup> Alexander Malafeev,<sup>⊥</sup> Viktor Ivanov,<sup>⊥</sup> Kurt Kremer,<sup>†</sup> Chad Risko,<sup>‡</sup> Jean-Luc Brédas,<sup>‡</sup> and Denis Andrienko<sup>†,\*</sup>

<sup>†</sup>Max Planck Institute for Polymer Research, Ackermannweg 10, 55128 Mainz, Germany

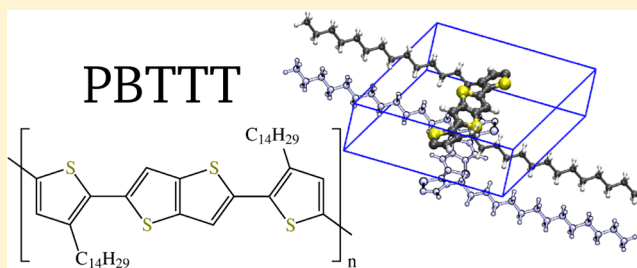
<sup>‡</sup>School of Chemistry and Biochemistry and Center for Organic Photonics and Electronics, Georgia Institute of Technology, Atlanta, Georgia 30332-0400, United States

<sup>§</sup>School of Materials Science and Engineering, Georgia Institute of Technology, Atlanta, Georgia 30332-0245, United States

<sup>⊥</sup>Physics Department, Moscow State University, Moscow, Russia

## Supporting Information

**ABSTRACT:** We establish a link between the microscopic ordering and the charge-transport parameters for a highly crystalline polymeric organic semiconductor, poly(2,5-bis(3-tetradecylthiophen-2-yl)thieno[3,2-*b*]thiophene) (PBTTT). We find that the nematic and dynamic order parameters of the conjugated backbones, as well as their separation, evolve linearly with temperature, while the side-chain dynamic order parameter and backbone paracrystallinity change abruptly upon the (also experimentally observed) melting of the side chains around 400 K. The distribution of site energies follows the behavior of the backbone paracrystallinity and can be treated as static on the time scale of a single-charge transfer reaction. On the contrary, the electronic couplings between adjacent backbones are insensitive to side-chain melting and vary on a much faster time scale. The hole mobility, calculated after time-averaging of the electronic couplings, reproduces well the value measured in a short-channel thin-film transistor. The results underline that to secure efficient charge transport in lamellar arrangements of conjugated polymers: (i) the electronic couplings should present high average values and fast dynamics, and (ii) the energetic disorder (paracrystallinity) should be small.



## I. INTRODUCTION

Thiophene-based conjugated polymers<sup>1</sup> show considerable potential as low-cost materials for solution-processed solar cells and thin-film transistors (TFTs).<sup>2–4</sup> A prototypical example is poly(2,5-bis(3-alkylthiophen-2-yl)thieno[3,2-*b*]thiophene) (PBTTT), the chemical structure of which is shown in Figure 1. Thin-film transistors (TFTs) with PBTTT as the active layer have demonstrated charge-carrier mobilities up to  $1 \text{ cm}^2 \text{V}^{-1} \text{s}^{-1}$  with good air stability;<sup>5–8</sup> however, as a donor material in bulk-heterojunction solar cells PBTTT has shown limited performance,<sup>9–11</sup> which is partially a function of the formation of an intercalated bimolecular complex.<sup>12</sup> Pristine

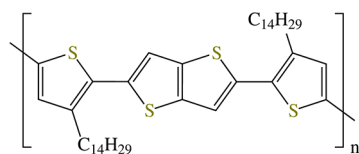


**Figure 1.** Chemical structure of poly(2,5-bis(3-tetradecylthiophen-2-yl)thieno[3,2-*b*]thiophene) (PBTTT- $\text{C}_{14}$ ) studied in this work.

PBTTT forms extended crystalline domains on crystallization from a liquid crystal phase.<sup>13</sup> Regioregularity and the large free-volume between adjacent alkyl chains facilitate its high degree of crystallinity with well-ordered alkyl side chains allowing for interdigitation and formation of closely packed lamellar structures.<sup>5</sup> The formation of such high-quality crystallites (promoted by the side-chain interdigitation) has been suggested to be directly related to the better performance of PBTTT in TFTs vs other polymers, rather than differences in trap energy/density or domain size.<sup>14</sup>

Considerable experimental and theoretical efforts have been undertaken to determine the molecular-scale packing of PBTTT. Initial structural analyses of the thin-film structure based on X-ray scattering assumed an orthorhombic unit cell.<sup>5,15</sup> This structural model was then further refined based on data from near-edge X-ray absorption fine structure and infrared absorption spectroscopy<sup>16</sup> as well as density functional

**Received:** November 11, 2012

**Revised:** January 4, 2013

**Published:** January 4, 2013

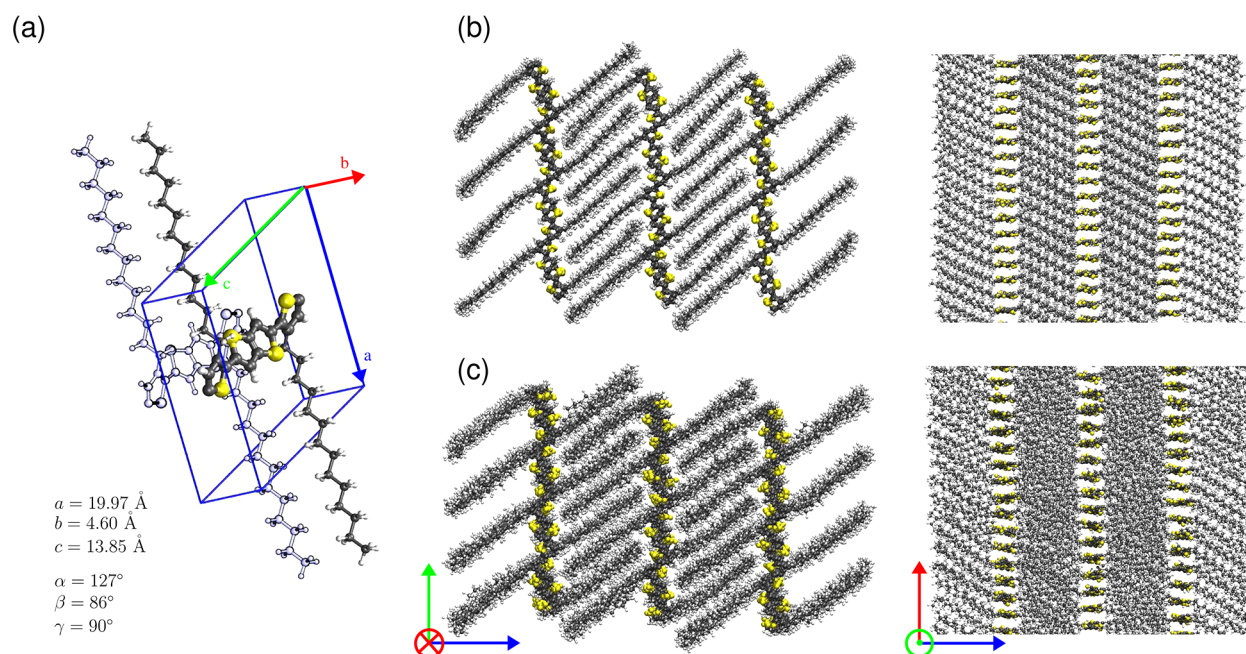


**Figure 2.** (a) PBTTC-C<sub>14</sub> primitive unit cell with cell parameters as obtained from molecular dynamics simulations. Projections along the  $\pi$ - $\pi$  stacking and chain directions at 300 K (b) and 500 K (c).

theory (DFT) calculations.<sup>17</sup> Furthermore, molecular mechanics and X-ray diffraction (XRD) simulations were used to study the molecular packing of the PBTTC-C<sub>12</sub> lamellae and resulted in the proposition of a triclinic unit cell.<sup>18</sup> An orthorhombic unit cell was again proposed for biaxially aligned films based on grazing incidence X-ray diffraction analysis.<sup>19</sup> Recently, a combined X-ray diffraction and molecular mechanics approach has been used to determine the triclinic nature of the unit cell of PBTTC-C<sub>*n*</sub> with  $n = 12, 14, 16$  for both uniaxial and biaxial alignments.<sup>20</sup> Periodic band-structure calculations were employed to evaluate the electronic structure of the crystalline domains; the results showed that, as expected, the band dispersions were largest along the polymer backbones though still significant along the  $\pi$ -stacking direction (in agreement with previous results<sup>17</sup>). This unit cell (see Figure 2) is used here to generate a starting supercell of a biaxially oriented film.

Charge-carrier transport in such semicrystalline polymers is controlled by a network of ordered regions (formed by the organization of the polymer backbones into two-dimensional lamella sheets) and disordered regions. An attempt to link charge mobility to molecular ordering (to be more precise, to the degree of paracrystalline disorder in the  $\pi$ -stacking direction) has recently been made by using X-ray line-shape analysis and a tight-binding model.<sup>17,21</sup> It was concluded that the static positional disorder, leading to a static disorder of the electronic coupling elements between adjacent backbones, results in a tail of trap states, with trap energies on the order of 0.1 eV. The static disorder in the electronic coupling elements was postulated in this model and the effect of the energetic disorder due to electrostatic and polarization effects was neglected. Additionally, the anisotropy of the charge-carrier transport in biaxially aligned PBTTC films using a zone-cast method has been studied by measuring the mobility parallel and perpendicular to the polymer chain direction.<sup>8</sup> The results suggest that the mobility along the polymer chain is larger than that in the  $\pi$ -stacking direction (which further substantiate the periodic band-structure results) and that mobilities in both

cases are thermally activated with an activation energy of 0.06–0.07 eV.

In this work, we aim to provide a rigorous, microscopic, link between the morphology and the charge-carrier transport parameters in the highly crystalline domains of PBTTC-C<sub>14</sub>. To do so, we first reparameterize the PBTTC force field and perform molecular-dynamics simulations of a  $3 \times 30 \times 4$  supercell for a range of temperatures. We then evaluate the electronic coupling elements and site-energy differences for pairs of molecules in a molecular-dynamics trajectory and establish correlations between their distributions and the dynamic, nematic, and paracrystallinity order parameters. By comparing the decay times of the respective autocorrelation functions to typical charge transfer times, we conclude that the electronic couplings must be preaveraged before calculating the charge-transfer rates, while static energetic disorder can be assumed on time scales of a single electron-transfer reaction. Finally, hole-transfer rates between neighboring polymer chains are evaluated and the charge-carrier dynamics are simulated within PBTTC-C<sub>14</sub> lamellae.

## II. MOLECULAR DYNAMICS

The force field for PBTTC is based on the OPLS-AA<sup>22</sup> force field with the bonded degrees of freedom reparameterized using the potential energy scans as described in the Supporting Information. Starting configurations were prepared using the triclinic unit cell shown in Figure 2a and described in ref 20. First, a tetramer was prepared with the terminal groups saturated with hydrogens. Then a supercell with three lamellae was generated, with each lamella containing 30 tetramers. Molecular dynamics simulations were performed in the NPT ensemble (anisotropic Berendsen barostat<sup>23</sup> and a canonical velocity-rescaling thermostat<sup>24</sup>) using the GRO-MACS simulation package.<sup>25</sup> A 2 ns equilibration followed by a 1 ns production run was performed in the 300–500 K temperature range (in steps of 50 K). For analysis, snapshots are saved at time intervals of 100 ps during the production run.

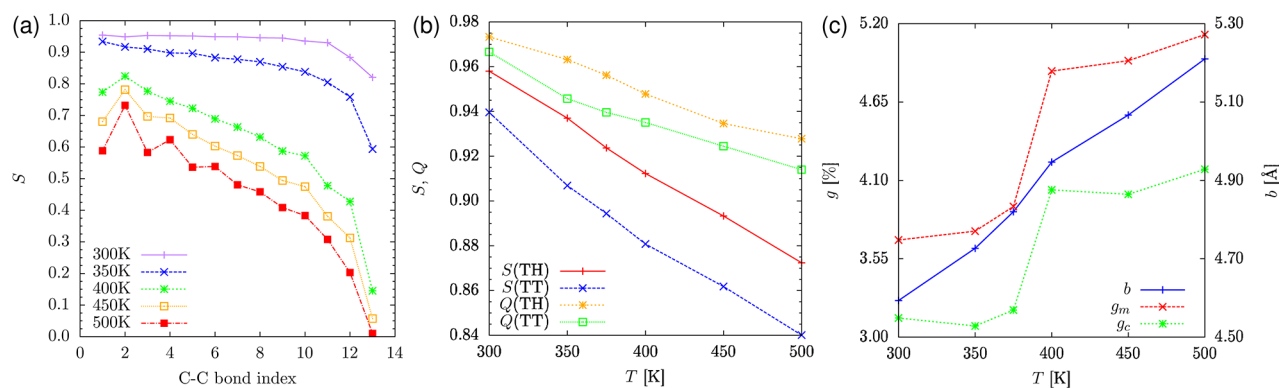


**Figure 3.** (a) Dynamic order of carbon–carbon bonds in aliphatic side-chains. (b) Static ( $Q$ ) and dynamic ( $S$ ) order parameters of thiophene (TH) and thienothiophene (TT) backbone motifs. (c) Temperature-resolved paracrystallinity  $g$  as well as expansion of unit cell  $b$  along  $\pi$ -stacking direction.

Two representative snapshots, equilibrated at 300 and 500 K are shown in Figure 2, parts b and c, respectively. As expected, both side chains and backbones become more mobile at higher temperatures, while the long-range order is preserved.

The increase in side-chain mobility was quantified by calculating the dynamic order parameters<sup>26,27</sup> which can also be extracted from solid-state NMR measurements:<sup>28,29</sup>

$$S = \left\langle \frac{1}{N} \sum_{i=1}^N \left( \frac{3}{2} (\bar{M}^{(i)} \cdot \bar{m}^{(i)})^2 - \frac{1}{2} \right) \right\rangle \quad (1)$$

where  $\bar{M}^{(i)} = \langle \bar{m}^{(i)} \rangle$ ,  $\langle \dots \rangle$  denotes time average,  $N$  is the number of molecules in the system,  $\bar{m}^{(i)}$  is the instantaneous vector of interest (e.g., the bond vector of neighboring carbons in the case of alkyl side chains).  $S = 1$  implies a constant in time for the bond orientation, while  $S < 1$  indicates that the orientation is changing over time. Note that the dynamic order parameter is calculated with respect to a time-averaged orientation of  $\bar{m}^{(i)}$ ; thus, for a system of *static* randomly oriented vectors, the dynamic order  $S$  equals one while the nematic order  $Q$ , as introduced in eq 2, is zero.

The dependence on temperature and bond position of the dynamic order parameter  $S$  is shown in Figure 3a for the alkyl side chains. As expected, side-chain mobility increases with increasing distance between the CC-bond of interest and the backbone, especially at higher temperatures. Interestingly, there is a sharp decrease of  $S$  between 350 and 400 K, in line with what would happen upon melting of crystalline side chains. Such transitions are not observed for the dynamic order parameters of the thiophenes and thienothiophenes along the backbone, Figure 3b, as these conjugated units become only slightly more mobile (torsional motion) at higher temperatures.

To assess the orientational ordering of the conjugated subunits in the polymer backbone, the nematic order parameter  $Q$ , i.e., the largest eigenvalue of the order parameter tensor,  $\hat{Q}$ , is calculated, where:

$$Q_{\alpha\beta} = \left\langle \frac{1}{N} \sum_{i=1}^N \left( \frac{3}{2} u_{\alpha}^{(i)} u_{\beta}^{(i)} - \frac{1}{2} \delta_{\alpha\beta} \right) \right\rangle \quad (2)$$

$N$  is the number of conjugated subunits (thiophene and thienothiophene rings) and  $\vec{u}^{(i)}$  denotes a vector perpendicular to the conjugated planes of these units.  $Q = 1$  implies perfect alignment of the unit vectors  $\vec{u}$  and  $Q = 0$  corresponds to an isotropic angular distribution.

The temperature dependence of the nematic order parameter is shown in Figure 3b both for the thiophene (TH) and thienothiophene (TT) units. The change in nematic ordering is rather small, i.e., the conjugated units of the backbone remain well aligned (but become more mobile upon increasing temperature). Both the nematic and dynamic order parameters of the backbone do not show any anomalies that could be linked to the abrupt increase of side-chain dynamics between 350 and 400 K.

Finally, to quantify the degree of positional disorder along the  $\pi$ -stacking direction, the paracrystallinity parameter,  $g_m$ , was evaluated as:

$$g_m^2 = \frac{\langle d_{hkl}^2 \rangle - \langle d_{hkl} \rangle^2}{\langle d_{hkl} \rangle^2} \quad (3)$$

where  $d_{hkl}$  is the distance between the centers of mass of two closest conjugated subunits belonging to different polymer chains, projected on the  $hkl$ -direction. Since we are interested in paracrystallinity along the  $\pi$ -stacking direction, i.e., along the  $\vec{b}$  vector,  $hkl$  corresponds to 010. Paracrystallinity can be extracted from X-ray diffraction data<sup>30</sup> and for PBTTT-C<sub>14</sub> the room temperature paracrystallinity is 7.3%.<sup>21</sup> The corresponding calculated value is 3.7%, smaller than that determined experimentally, and implies that the backbone is not perfectly crystalline even in highly crystalline regions of PBTTT-C<sub>14</sub>.

The temperature dependence of the paracrystallinity along the  $\pi$ -stacking direction is shown in Figure 3c, together with the corresponding unit-cell-vector expansion. One can see that a virtually linear thermal expansion of the cell is accompanied by a steep increase in paracrystallinity between 350 and 400 K. Remarkably, this is the only order parameter that clearly reflects the enhanced side-chain dynamics. A paracrystallinity parameter  $g_c$  calculated from whole chains instead of individual monomers exhibits the same behavior while excluding contributions from increased disorder in torsional degrees of freedom. This suggests that the main contribution to fluctuations in the (inter) monomer–monomer distances results from breathing modes along the  $\pi$ -stacking direction, where the centers-of-mass of whole chains undergo shifts. The difference  $\Delta g = g_m - g_c$  increases linearly with temperature (not shown), with only a minor kink of the same intensity as for the nematic order parameter  $Q$ (TH) occurring at 400 K. This underlines that  $g_c$  does not include the increase in paracrystallinity due to thermal motion of backbone torsional

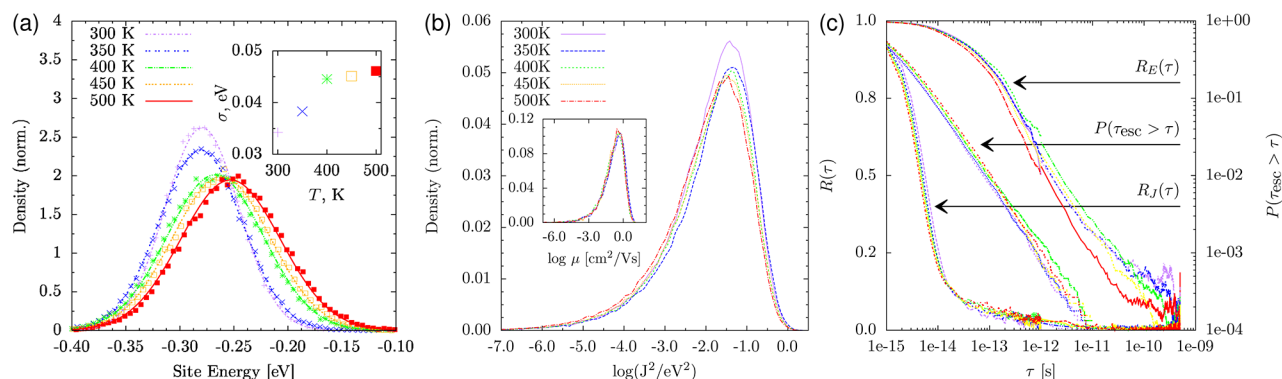


**Figure 4.** Temperature-resolved distributions of (a) site energies and (b) electronic coupling elements for a trajectory obtained using 1000 molecular dynamic snapshots, with distribution of lamellar mobilities shown in the inset. Distributions of site energies and pair couplings have been calculated for the same number of sites and pairs, respectively, and are hence implicitly normalized. (c) Time autocorrelation functions for site energies and electronic coupling elements; these functions are compared to the distribution of average escape times. The color-coding of the temperature range is the same as in parts a and b.

degrees of freedom and hence documents the pure effect of side-chain melting on the conjugated planes.

A structural transition around 410 K has also been observed experimentally for PBTTT-C<sub>14</sub>; Fourier-transform infrared spectroscopy data established the link between this transition and the melting of the side chains.<sup>31,32</sup> Here, apart from the linear thermal expansion along the  $\pi$ -stacking direction and a jump in *inter*-lamellar separation, both of which are observed in our simulations, no abrupt change, either in torsional disorder affecting the conjugation length or in conjugated-plane orientation, could be detected. However, to the best of our knowledge, there has been no experimental study to date of the temperature-dependent paracrystallinity in PBTTT-C<sub>14</sub>.

To summarize, the dynamic and nematic order parameters of the polymer backbones as well as the unit-cell dimensions display a weak linear dependence on temperature. In contrast, the side-chain dynamic order parameter and paracrystallinity along the  $\pi$ -stacking direction both exhibit an abrupt change within the 350–400 K range due to side-chain melting. In what follows, we evaluate how these structural changes affect the electronic coupling elements, site energies, (interchain) charge-transfer rates, and ultimately charge-carrier mobilities.

### III. ENERGETIC DISORDER

With the molecular dynamics trajectories at hand, we now turn to an evaluation of the electrostatic contribution to site energies. This contribution is due to a locally varying electrostatic potential and is calculated self-consistently using the Thole model<sup>33</sup> on the basis of the atomic polarizabilities and partial charges for a cation and a neutral molecule listed in the Supporting Information.

The distributions in hole site energies, i.e., the differences between the energies of the system when a selected molecule is in the cationic or neutral state, are shown in Figure 4a, together with the fits to a Gaussian function:

$$f(E; \mu, \sigma^2) = \frac{1}{\sqrt{2\pi}\sigma} \exp\left[-\frac{1}{2}\left(\frac{E - \mu}{\sigma}\right)^2\right] \quad (4)$$

The distributions both broaden and shift to higher energies with increasing temperature. Note that the shift of the mean of the distribution is not essential for a one-component system, since only site-energy *differences* enter in the Marcus-rate expression, eq 6. Instead, it is the broadening that is crucial

here, and, notably, even for a perfect crystalline molecular arrangement, small thermal fluctuations of the backbone torsional angles (note that the side chains are not accounted for when evaluating the site energies) lead to energetic disorder in the system. This disorder increases at higher temperatures, with a clearly distinct temperature dependence below 350 K and above 400 K (see the inset in Figure 4a), which correlates with the abrupt decrease in side-chain dynamic order parameter and paracrystallinity, shown in Figure 3a,c. In the next section, it will be shown that this disorder can be treated as *static* on the time scale of an electron-transfer reaction.

### IV. ELECTRONIC COUPLINGS

We now consider the distribution of the electronic coupling elements that enter the rates of electron tunneling between the diabatic states  $\phi^i$ ,  $\phi^j$  of the charge-transfer complex.<sup>34</sup> These diabatic states are constructed from the highest occupied molecular orbital of a DFT optimized PBTTT tetramer. To account for the variation of dihedral angles along the polymer backbone, the orbitals are rotated into the respective coordinate frames of the thiophene and thienothiophene fragments. Even for large couplings, this choice of the reference states has been shown to predict similar values of charge-carrier mobilities as schemes that do not assume charge localization,<sup>35</sup> and is expected to result here from the non-negligible energetic disorder. The electronic coupling elements,  $J_{ij} = \langle \phi^i | \hat{H}_{ij} | \phi^j \rangle$ , with  $\hat{H}_{ij}$  the dimer Hamiltonian, are calculated for each molecular pair (*ij*) from the neighbor list using the semiempirical ZINDO method.<sup>36,37</sup> A pair of molecules is added to the list of neighbors if the distance between the centers-of-mass of any of the thiophene or thienothiophene groups is below a cutoff of 0.5 nm. This small, fragment-based cutoff insures that only nearest neighbors are added to the neighbor list.

The distributions of electronic coupling elements, shown in Figure 4b, shift toward smaller values at higher temperatures due to the thermal expansion of the unit cell along the  $\pi$ -stacking direction (see Figure 3c). This, as will be shown later, does not affect significantly the charge-carrier mobility. In spite of a crystalline order, there is a broad tail of very small couplings, down to 10<sup>-4</sup>eV, even though only nearest neighbors are present in the neighbor list. Since the transport has a one-dimensional character, it can be anticipated that a broad distribution of electronic couplings limits charge mobility along lamellae. Indeed, the inset of Figure 4b shows that mobility

values, evaluated for all molecular-dynamics snapshots, are similarly distributed, with small mobilities as low as  $10^{-6}\text{cm}^2/(\text{Vs})$ . This would obviously result in rather small average mobility values. However, this conclusion is valid only if charge-carrier transport were to occur within a static snapshot of the system; in reality, both transfer integrals and site energies are time-dependent. In fact, a broad distribution of electronic couplings is linked to variations in the backbone dihedral angles. The thermal motion of these angles presents typical relaxation times of 100 fs and hence can be slower than the time required for an electron-transfer reaction.

In order to understand whether such a static picture can be used in our case, in the next section we evaluate the distributions in relaxation times of the electronic coupling elements and site energies and compare them to the distribution of escape times of a charge carrier.

## V. AUTOCORRELATION FUNCTIONS

To explore the limitations associated with simulating charge transfer in a frozen morphology, we compare charge escape times ( $\tau_{\text{esc}}$ , defined below) to relaxation times of the backbone as reflected both in the electronic coupling elements and site energies.

Escape rates are defined as  $\Gamma_{\text{esc}}^{(i)} = \sum_{j(i)} \Gamma_{ij}$  where  $\Gamma_{ij}$  is the hole-transfer rate from site  $i$  to site  $j$ , and the sum is evaluated for all nearest neighbors  $j$  of site  $i$ . The escape time, i.e., the average time a charge spends localized on a given site, can then be obtained as  $\tau_{\text{esc}}^{(i)} = 1/\Gamma_{\text{esc}}^{(i)}$ . From the resulting distribution of escape times,  $p(t)$ , we calculate the distribution (exceedence, or complementary cumulative distribution function),  $P(\tau) = \int_{\tau}^{\infty} p(t) dt$ , which is proportional to the number of sites with an escape time larger than  $\tau$ .

Backbone dynamics are estimated from the time autocorrelation functions  $R_E(\tau)$  for site energies  $E^{(i)}$  and  $R_j(\tau)$  for transfer amplitudes  $|J_{ij}|^2$ :

$$R_E(\tau) = \frac{\langle (E_t^{(i)} - \mu)(E_{t+\tau}^{(i)} - \mu) \rangle}{\sigma^2} \quad (5)$$

where  $\langle \dots \rangle$  denotes the ensemble average; the width  $\sigma$  and average  $\mu$  have the same meaning as in the electronic density of states, eq 4. The analogous expression is used for the transfer integrals.

The autocorrelation functions are shown along with the tail distribution of escape times in Figure 4c. Interestingly, the relaxation of the electronic coupling elements occurs on significantly shorter time scales than for site energies. This reflects their dissimilar physical origins: Site energies are related to long-range electrostatic interactions where averaging occurs over a large number of nearest neighbors and leads to spatial correlations. On the other hand, the electronic coupling elements (to a first approximation) only depend on the geometries of pairs of molecules, which results in increased sensitivity to thermal motions of the internal degrees of freedom.

For intermediate delay times ( $\tau$  on the order of femtoseconds for  $|J_{ij}|^2$  and picoseconds for  $E^{(i)}$ ), both  $R_j(\tau)$  and  $R_E(\tau)$  decay exponentially. Around  $\tau = 10$  fs,  $R_j(\tau)$  features a crossover to a regime that still presents an exponential correlation decay but with a significantly increased time constant. We estimate a decorrelation time  $\tau_j \approx 15$  fs from the intersection of the two exponentials.

These two time scales,  $\tau_j$  and  $\tau_E$ , should be compared to the tail distribution of escape times,  $P(\tau)$ . On a log–log scale, the linear shape for large  $\tau$  implies a power-law decay  $P(\tau) \sim O(1/\tau)$ . Hence, reducing the tail distribution to just one time scale to be compared to  $\tau_E$  or  $\tau_j$  is not possible (the majority of sites has an escape time far smaller than any relaxation time, but it is the sites in the tail of the exceedence that act as shallow or deep traps and significantly slow down transport). Still, to allow for a partial separation of time scales, it can be stated that a significant fraction of sites (5%) traps charges for a time on average longer than  $\tau_j$ , whereas only a very small fraction (around 0.001% by extrapolation) exceeds the long-time limit set by  $\tau_E$ .

We therefore conclude that charge-carrier dynamics is in practice limited by the backbone dynamics, since relaxation times of electronic couplings due to thermal fluctuations exceed typical time scales of hopping transport in the system. To some extent, it is still possible to resort to a single charge-transfer rate to describe transport, eq 6, and use a time-average for all pair electronic couplings. In fact, a similar conclusion has been reached for columnar discotic liquid crystals,<sup>38</sup> where one-dimensional transport and fast molecular motions (librations and rotations) led to rapid changes in electronic couplings. As an aside, we note that it is also possible to accurately account for the explicit time-dependence of electronic couplings by employing semiclassical dynamics.<sup>35,39</sup>

## VI. CHARGE TRANSPORT

We finally study charge transport along the  $\pi$ -stacking (010) direction, as this is expected to be the rate-limiting charge-transport direction. To do this, charge-transfer rates are computed using the high-temperature limit of the semiclassical Marcus charge-transfer theory<sup>27,40</sup>

$$\omega_{ij} = \frac{J_{ij}^2}{\hbar} \sqrt{\frac{\pi}{\lambda_{ij} k_B T}} \exp \left[ -\frac{(\Delta E_{ij} - \lambda_{ij})^2}{4\lambda_{ij} k_B T} \right] \quad (6)$$

where  $T$  denotes the temperature;  $J_{ij}$ , the electronic coupling element between molecules  $i$  and  $j$ ;  $\Delta E_{ij}$ , the site energy difference; and  $\lambda_{ij}$ , the reorganization energy. Reorganization energies  $\lambda_{ij}$  were evaluated via density functional theory (DFT) from the potential energy surfaces of a single molecule in a cationic and neutral state using the B3LYP functional and the 6-311(d,p) basis set. The values are summarized in tab. I for a

**Table I. Reorganization Energies (in eV) of a Chain of  $n$  Repeat Units Calculated Using Potential Energy Surfaces of the Geometry-Optimized (opt) and Constrained in a Plane PBTTT Backbone<sup>a</sup>**

$n$	1	2	3	4	5	6
$\lambda_{\text{opt}}$	0.516	0.378	0.306	0.239	0.131	0.098
$\lambda_{\text{con}}$	0.304	0.231	0.176	0.131	0.098	0.084

<sup>a</sup>B3LYP functional, 6-311g(d,p) basis set.

geometry-optimized backbone ( $\lambda_{\text{opt}}$ ) and for a planar (constrained) backbone ( $\lambda_{\text{con}}$ ). Since in a PBTTT crystal the backbone is planar and large deviations from planarity are restrained by nonbonded interactions with neighboring chains,  $\lambda_{\text{con}} = 0.131$  eV of a tetramer was used to evaluate the rates. Electronic couplings and site-energy differences were calculated explicitly for each pair of molecules using quantum-mechanical

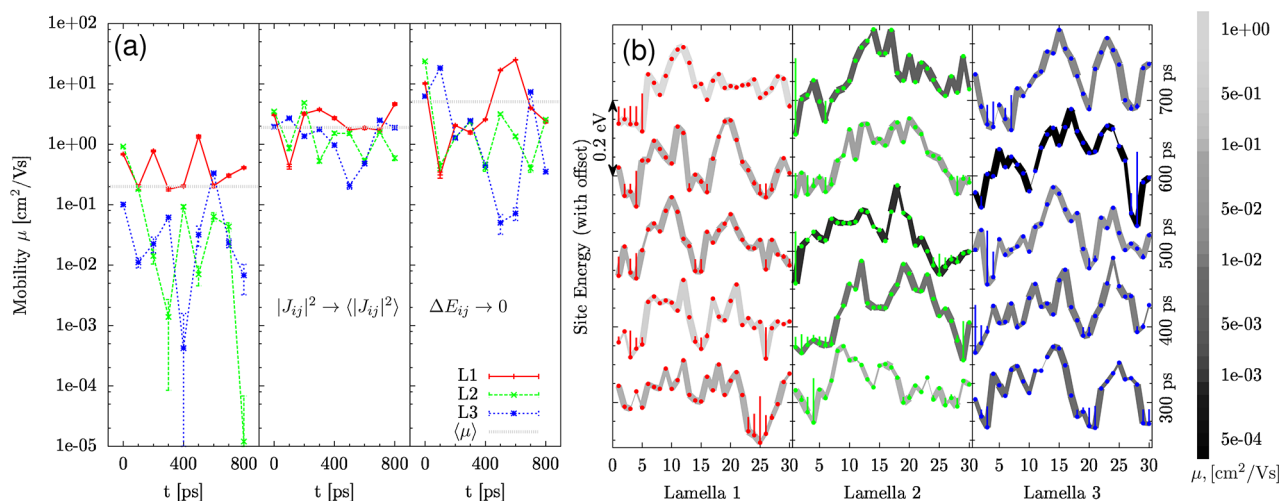


**Figure 5.** (a) Charge carrier mobilities for three lamellae and 10 molecular dynamics snapshots. Left: static picture. Center: preaveraged electronic coupling elements. Right: without energetic disorder. (b) Energetic landscape for three lamellae and five molecular dynamics snapshots. Bonds connecting hopping sites have width proportional to the logarithm of squared electronic coupling elements. Line color reflects the charge-carrier mobility of the lamella. Vertical bars reflect the occupation probability of a site. Results shown are for 300 K.

or polarizable force-field methods<sup>41</sup> as described in sections III and IV.

Charge-carrier dynamics was modeled by solving the master equation for a charge carrier drift-diffusion in an applied electric field. All charge transport calculations were performed using the VOTCA package.<sup>41</sup>

Single-carrier mobilities for all three lamellae in the simulation box as a function of MD simulation time are shown in Figure 5a. As simulations at higher temperatures are qualitatively similar, we show results for 300 K only. Indeed, in this system, the mobility exhibits no temperature dependence in spite of the increase in energetic disorder, since larger energy barriers are effectively mitigated due to the elevated temperature. When  $\mu$  is calculated using static snapshots, it presents large variations both from snapshot to snapshot and from lamella to lamella (approximately 5 orders of magnitude), with an average value of 0.2 cm<sup>2</sup>/(Vs). If we now account for fast variations of electronic couplings and average their squares for every pair before calculating the rates, the fluctuations of  $\mu$  decrease (see the middle pane in Figure 5a) and the average mobility increases to 1.1 cm<sup>2</sup>/(Vs), which is in a good agreement with the experimentally measured value of 0.9 cm<sup>2</sup>/(Vs) for a TFT with a short channel.<sup>6,7</sup>

One might conclude at this point that small electronic couplings represent the only limiting factor for one-dimensional transport. This, however, is only partially correct. If we remove the energetic disorder from the system, i.e., assume that  $\Delta E_{ij} = 0$  for all sites, the mobility variation becomes much smaller than in the static case, even without averaging of electronic couplings. The average value also increases, to 1.9 cm<sup>2</sup>/(Vs). Hence, even though the energetic disorder is small, when combined with the one-dimensional character of transport, it leads to a substantial reduction of charge mobility. Or, in other words, a single energetic trap can impede transport through the entire lamella.<sup>42</sup>

This effect is visualized in Figure 5b, where the energetic landscape is shown for three lamellae at five different simulation times. Here, the widths of the bonds connecting the hopping sites are proportional to squared electronic coupling elements, while the heights of the vertical bars are proportional to the occupation probability of a specific site. The gray scale indicates

the average mobility of a particular lamella, with darker colors corresponding to lower mobilities. One can see that site energies are spatially correlated and almost every landscape has a trap of ca. 0.2 eV, where the charge is localized most of the time (trap sites have high occupation probability). In fact, since the site-energy dynamics is significantly slower than the carrier transport dynamics, the effect of energetic disorder is potentially more harmful for the efficiency of one-dimensional transport. It might indeed happen that, for larger widths of the energetic disorder, the limiting factor for hole transfer will be the dynamics of energetic traps existing in the system due to thermal fluctuations of the molecular structure.

## VII. CONCLUSIONS

To summarize, we have studied the temperature dependence of the dynamic disorder in the crystalline lamellar arrangement of the conjugated polymer, PBTTT-C<sub>14</sub>. This disorder has been characterized by three order parameters: dynamic, nematic, and paracrystallinity. An abrupt decrease of the side-chain dynamic order, observed around 400 K, correlates well with a sharp increase of the backbone paracrystallinity, while all nematic and dynamic order parameters of the backbone as well as the unit-cell expansion along the  $\pi$ -stacking direction show a monotonic linear temperature dependence.

The morphological disorder leads to broadening of distributions of the electronic coupling elements and site energies. The variation in electronic couplings was found to occur on a much faster time scale (hundreds of femtoseconds) than a typical time required for a single electron-transfer event. Hence, the electronic coupling elements were preaveraged before calculating electron-transfer rates. Site energies, by contrast, were found to change on a significantly slower scale and thus could be treated as static on the time scale of charge transport.

Finally, the calculated charge-carrier mobilities are found to be in very good agreement with the experimentally measured values in a short channel TFT. Preaveraging the electronic couplings (due to their fast dynamics) leads to a factor of 5 increase in the average mobility.

On the basis of these calculations, an important conclusion is that, in order to secure polymeric organic semiconductors with large charge-carrier mobilities, it is not enough to have large electronic coupling averages. In addition, the fast time-scale dynamics of the polymers and, even more importantly, the small energetic disorder (which evolves on a much slower than the charge-carrier dynamics time scale) are desirable. From the point of view of chemical design, it should be noted that the alkyl side chains that are added for solubility purposes can affect the backbone paracrystallinity and hence increase the energetic disorder if they do not remain in a highly crystalline state. It is therefore important that both backbones and side chains maintain good crystalline order.

## ■ ASSOCIATED CONTENT

### ■ Supporting Information

Atomistic simulations, force-field parameters, and details of charge transport simulations. This material is available free of charge via the Internet at <http://pubs.acs.org>.

## ■ AUTHOR INFORMATION

### Corresponding Author

\*E-mail: [denis.andrienko@mpip-mainz.mpg.de](mailto:denis.andrienko@mpip-mainz.mpg.de).

### Notes

The authors declare no competing financial interest.

## ■ ACKNOWLEDGMENTS

The work in Mainz was partly supported by the DFG programs IRTG 1328 and SPP 1355, and BMBF grants MESOMERIE and MEDOS. The work at Georgia Tech was supported by the Center for Advanced Molecular Photovoltaics funded through the King Abdullah University of Science and Technology (KAUST). We are grateful to Björn Baumeier, Pascal Korrdt, Anton Melnyk, Kostas Daoulas, Patrick Gemünden, and Mara Jochum for critical reading of the manuscript.

## ■ REFERENCES

- (1) McCullough, R. D. *Adv. Mater.* **1998**, *10* (2), 93–116.
- (2) McCulloch, I.; Heeney, M.; Chabiny, M. L.; De-Longchamp, D.; Kline, R. J.; Coelle, M.; Duffy, W.; Fischer, D.; Gundlach, D.; Hamadani, B.; Hamilton, R.; Richter, L.; Salleo, A.; Shkunov, M.; Sporrowe, D.; Tierney, S.; Zhong, W. *Adv. Mater.* **2009**, *21* (10–11), 1091–1109.
- (3) Boudreault, P.-L. T.; Najari, A.; Leclerc, M. *Chem. Mater.* **2010**, *23* (3), 456–469.
- (4) McCulloch, I.; Ashraf, R. S.; Biniek, L.; Bronstein, H.; Combe, C.; Donaghey, J. E.; James, D. I.; Nielsen, C. B.; Schroeder, B. C.; Zhang, W. *Acc. Chem. Res.* **2012**, *45* (5), 714–722.
- (5) McCulloch, I.; Heeney, M.; Bailey, C.; Genevicius, K.; MacDonald, I.; Shkunov, M.; Sparrowe, D.; Tierney, S.; Wagner, R.; Zhang, W.; Chabiny, M. L.; Kline, R. J.; McGehee, M. D.; Toney, M. F. *Nat. Mater.* **2006**, *5* (4), 328–333.
- (6) Hamadani, B. H.; Gundlach, D. J.; McCulloch, I.; Heeney, M. *Appl. Phys. Lett.* **2007**, *91*, 24.
- (7) Umeda, T.; Kumaki, D.; Tokito, S. *J. Appl. Phys.* **2009**, *105* (2), 024516–024516–5.
- (8) Lee, M. J.; Gupta, D.; Zhao, N.; Heeney, M.; McCulloch, I.; Sirringhaus, H. *Adv. Funct. Mater.* **2011**, *21* (5), 932–940.
- (9) Parmer, J. E.; Mayer, A. C.; Hardin, B. E.; Scully, S. R.; McGehee, M. D.; Heeney, M.; McCulloch, I. *Appl. Phys. Lett.* **2008**, *92* (11), 113309–113309–3.
- (10) Mayer, A. C.; Toney, M. F.; Scully, S. R.; Rivnay, J.; Brabec, C. J.; Scharber, M.; Koppe, M.; Heeney, M.; McCulloch, I.; McGehee, M. D. *Adv. Funct. Mater.* **2009**, *19* (8), 1173–1179.

- (11) Rance, W. L.; Ferguson, A. J.; McCarthy-Ward, T.; Heeney, M.; Ginley, D. S.; Olson, D. C.; Rumbles, G.; Kopidakis, N. *ACS Nano* **2011**, *5* (7), 5635–5646.
- (12) Miller, N. C.; Cho, E.; Junk, M. J. N.; Gysel, R.; Risko, C.; Kim, D.; Acevedo-Feliz; Knox, C.; Michael Ryan, H.; Dudenko, D.; Chmelka, B. F.; Toney, M.; Brédas, J. L.; McGehee, M. D. *Adv. Mater.* **2012**, *24*, 6071–6079.
- (13) Schuettfort, T.; Watts, B.; Thomsen, L.; Lee, M.; Sirringhaus, H.; McNeill, C. R. *ACS Nano* **2012**, *6* (2), 1849–1864.
- (14) Wang, C.; Jimison, L. H.; Goris, L.; McCulloch, I.; Heeney, M.; Ziegler, A.; Salleo, A. *Adv. Mater.* **2010**, *22* (6), 697–701.
- (15) Chabiny, M. L.; Toney, M. F.; Kline, R. J.; McCulloch, I.; Heeney, M. *J. Am. Chem. Soc.* **2007**, *129* (11), 3226–3237.
- (16) DeLongchamp, D. M.; Kline, R. J.; Lin, E. K.; Fischer, D. A.; Richter, L. J.; Lucas, L. A.; Heeney, M.; McCulloch, I.; Northrup, J. E. *Adv. Mater.* **2007**, *19* (6), 833–837.
- (17) Northrup, J. E. *Phys. Rev. B* **2007**, *76* (24), 245202.
- (18) Brocorens, P.; Van Vooren, A.; Chabiny, M. L.; Toney, M. F.; Shkunov, M.; Heeney, M.; McCulloch, I.; Cornil, J.; Lazzaroni, R. *Adv. Mater.* **2009**, *21* (10–11), 1193–1198.
- (19) DeLongchamp, D. M.; Kline, R. J.; Jung, Y.; Germack, D. S.; Lin, E. K.; Moad, A. J.; Richter, L. J.; Toney, M. F.; Heeney, M.; McCulloch, I. *ACS Nano* **2009**, *3* (4), 780–787.
- (20) Cho, E.; Risko, C.; Kim, D.; Gysel, R.; Cates Miller, N.; Breiby, D. W.; McGehee, M. D.; Toney, M. F.; Kline, R. J.; Brédas, J. L. *J. Am. Chem. Soc.* **2012**, *134* (14), 6177–6190.
- (21) Rivnay, J.; Noriega, R.; Northrup, J. E.; Kline, R. J.; Toney, M. F.; Salleo, A. *Phys. Rev. B* **2011**, *83* (12), 121306.
- (22) Jorgensen, W. L.; Tirado-Rives, J. *J. Am. Chem. Soc.* **1988**, *110* (6), 1657–1666.
- (23) Berendsen, H. J. C.; Postma, J. P. M.; van Gunsteren, W. F.; DiNola, A.; Haak, J. R. *J. Chem. Phys.* **1984**, *81* (8), 3684.
- (24) Bussi, G.; Donadio, D.; Parrinello, M. *J. Chem. Phys.* **2007**, *126* (1), 014101.
- (25) Hess, B.; Kutzner, C.; van der Spoel, D.; Lindahl, E. *J. Chem. Theory Comput.* **2008**, *4* (3), 435–447.
- (26) Marcon, V.; Breiby, D. W.; Pisula, W.; Dahl, J.; Kirkpatrick, J.; Patwardhan, S.; Grozema, F.; Andrienko, D. *J. Am. Chem. Soc.* **2009**, *131* (32), 11426–11432.
- (27) May, F.; Marcon, V.; Hansen, M. R.; Grozema, F.; Andrienko, D. *J. Mater. Chem.* **2011**, *21* (26), 9538.
- (28) Hansen, M. R.; Graf, R.; Sekharan, S.; Sebastiani, D. *J. Am. Chem. Soc.* **2009**, *131* (14), 5251–5256.
- (29) Hansen, M. R.; Schnitzler, T.; Pisula, W.; Graf, R.; Mullen, K.; Spiess, H. W. *Angew. Chem., Int. Ed.* **2009**, *48* (25), 4621–4624.
- (30) Bonart, R.; Hosemann, R.; McCullough, R. *Polymer* **1963**, *4*, 199–211.
- (31) DeLongchamp, D. M.; Kline, R. J.; Jung, Y.; Lin, E. K.; Fischer, D. A.; Gundlach, D. J.; Cotts, S. K.; Moad, A. J.; Richter, L. J.; Toney, M. F.; Heeney, M.; McCulloch, I. *Macromolecules* **2008**, *41* (15), 5709–5715.
- (32) Miller, N. C.; Gysel, R.; Miller, C. E.; Verploegen, E.; Beiley, Z.; Heeney, M.; McCulloch, I.; Bao, Z.; Toney, M. F.; McGehee, M. D. *J. Polym. Sci., Part B: Polym. Phys.* **2011**, *49* (7), 499–503.
- (33) Thole, B. *Chem. Phys.* **1981**, *59* (3), 341–350.
- (34) May, V.; Kühn, O. *Charge and Energy Transfer Dynamics in Molecular Systems*, 3rd revised and enlarged ed.; Wiley-VCH: New York, 2011.
- (35) Vehoff, T.; Baumeier, B.; Troisi, A.; Andrienko, D. *J. Am. Chem. Soc.* **2010**, *132* (33), 11702–11708.
- (36) Brédas, J. L.; Calbert, J. P.; Filho, D. A. d. S.; Cornil, J. *Proc. Natl. Acad. Sci. U.S.A.* **2002**, *99* (9), 5804–5809.
- (37) Coropceanu, V.; Cornil, J.; da Silva Filho, D. A.; Olivier, Y.; Silbey, R.; Brédas, J. L. *Chem. Rev.* **2007**, *107* (4), 926–952.
- (38) Olivier, Y.; Muccioli, L.; Lemaire, V.; Geerts, Y. H.; Zannoni, C.; Cornil, J. *J. Phys. Chem. B* **2009**, *113* (43), 14102–14111.
- (39) Vehoff, T.; Chung, Y. S.; Johnston, K.; Troisi, A.; Yoon, D. Y.; Andrienko, D. *J. Phys. Chem. C* **2010**, *114* (23), 10592–10597.
- (40) Marcus, R. A. *Rev. Mod. Phys.* **1993**, *65* (3), 599.

- (41) Rühle, V.; Lukyanov, A.; May, F.; Schrader, M.; Vehoff, T.; Kirkpatrick, J.; Baumeier, B.; Andrienko, D. *J. Chem. Theory Comput.* **2011**, *7* (10), 3335–3345.
- (42) Scher, H.; Alexander, S.; Montroll, E. W. *Proc. Natl. Acad. Sci. U.S.A.* **1980**, *77* (7), 3758–3762.